Arabian Journal of Geosciences (2021) 14: 609
https://doi.org/10.1007/s12517-021-06944-4

ORIGINAL PAPER

Energy analysis and determination of controlling mechanisms of dissociation for hydrate reservoirs via tracking of dissociation front

Shadman Hasan Khan[1] · Gaurav Dixit[2] · Chandrajit Balo Majumder[3] · Amit Arora[4]

Received: 23 September 2020 / Accepted: 11 March 2021 / Published online: 26 March 2021

Abstract

A number of dissociation techniques like depressurization, thermal stimulation, CO2 exchange, etc. have been reported and investigated for natural gas hydrates in literature. However, dissociation of hydrate reservoirs is a complex process that is actually governed by several parameters. Hence, when inspected closely, the dissociation characteristics are a reflection of how these parameters are interlinked with each other. The present study is designed to numerically simulate a matrix of 21 different cases, which comprises an in-depth analysis for thermal stimulation, drawdown pressure, permeability, intrinsic rate constant, and thermal conductivity. The focus of the current study is motivated by practical interest, which aims at deciphering the associated mechanisms with hydrate dissociation. Over the years, different researchers have outlined the role of mechanisms such as heat transfer (HT), fluid flow (FF), and dissociation (D). The governing mechanisms are deduced through mathematical fitting and plotting of thermodynamic parameters for deciphering associated mechanisms. A "characteristic exponent" is determined for each of the cases to identify and delineate the different mechanisms for each of the 21 cases. Further, energy conversion from hydrate and energy quantification has been described in detail. As such, this information pool about hydrate dissociation is vital and necessary for efficient energy harvesting from hydrate reservoirs from varied geological settings and composition.

Keywords Natural gas hydrate · Energy recovery · Heat transfer · Hydrate dissociation · Fluid flow · Permeability

Introduction

In order to recover energy from gas hydrates, it is necessary to understand the gravity of parameters associated with hydrate dissociation. When these set of parameters are investigated, an interesting flow of information occurs, which reveals crucial information regarding how dissociation proceeds within the hydrate reservoir. Such a study benefits the practical interest of energy harvesting from hydrate reservoirs with varying thermodynamic and geological parameters. These parameters mainly include thermal conductivity (Castaldi et al. 2006), permeability (Tsypkin 1991, 1993), hydrate saturation (Yousif et al. 1990; Castaldi et al. 2006), rate constant, wellbore heating, drawdown pressure (Ahmadi et al. 2007a, b), etc. During the dissociation process, the hydrate reservoir can be distinguished either sharply or approximately into two distinct zones where, in one zone, hydrate has completely dissociated and, in the other zone, hydrate is more or less un-dissociated. These two regions are separated by a transition region, which is termed as the dissociation front. A number of investigations based on dissociation front have been carried out by different researchers based on analytical models (Selim and Sloan 1985, 1990; Ji et al. 2001; Ahmadi et al. 2007a),

Responsible Editor: Murat Karakus

✉ Shadman Hasan Khan
skhan1@ch.iitr.ac.in

[1] Department of Chemical Engineering, Indian Institute of Technology, Roorkee 247667, India

[2] Gas Hydrate Research & Technology Centre, Panvel, Mumbai 410106, India

[3] Indian Institute of Technology, Roorkee 247667, India

[4] Shaheed Bhagat Singh State Technical Campus, Firozpur 152004, India

numerical simulations (Castaldi et al. 2006; Bai and Li 2010; Konno et al. 2010; Li et al. 2014), and experiments (Ullerich et al. 1987; Yousif et al. 1991; Li et al. 2012)

With regard to the progression of dissociation front, the progression characteristics have been classified into two main types, i.e., piston type (Castaldi et al. 2006; Zhang et al. 2010) and non-piston type (Du et al. 2007; DU et al. 2008; Hong and Pooladi-Darvish 2018) Several researchers have highlighted these characteristics of dissociation front. Ahmadi et al. (2007a) used their analytical model to propose that dissociation front varies as a function of the square root of time.

A number of recent studies have established the benefit of numerical studies toward better inferring underlying dissociation mechanisms. Extraction technologies like thermal stimulation and depressurization (Rice 2003) along with their dependence upon heat transfer and fluid flow (Hamaguchi et al. 2007) were investigated. The different scenarios emerging due to the dominance of different mechanisms were numerically reproduced by Shi et al. (2018) through their robust numerical model. An in-depth study targeting the crucial role of heat flux (Uddin et al. 2008a) and kinetics (Uddin et al. 2008b) of hydrate dissociation and growth was performed by Uddin et al. (2008a, b).

As mentioned previously, the dissociation behavior changes with thermal conductivity, depressurization, particle size, permeability, thermal stimulation, and intrinsic rate constant (Li et al. 2020). Therefore, it is necessary to understand the shift which occurs due to the variation of the aforementioned parameters. The present study is designed to explore this gap in literature.

Further, a significant gap in the literature exists regarding the determination of "dominant" hydrate dissociation mechanisms, namely, heat transfer, fluid flow, and dissociation. Previous works describing mechanisms in a discrete manner include that of Kim et al. (1987) (intrinsic kinetics only). Their model was improved upon by Selim and Sloan (1989) (conductive heat transfer and fluid flow), Jamaluddin et al. (1989) (heat transfer and dissociation kinetics), and Yousif et al. (1991) (fluid flow of gas, water, and intrinsic kinetics). A more definitive work was accomplished by Moridis (2003) and Hong et al. (2003), who developed numerical and analytical models that featured fluid flow, heat transfer, dissociation kinetics, and accounting for porous media.

The present study addresses the need for a "criterion" to identify the dominant hydrate dissociation mechanisms for a particular case. As such, this information is identified by considering the wide variety of features in dissociation front have been reported by Ullerich et al. (1987), Selim and Sloan (1990), Yousif et al. (1991), Ahmadi et al. (2007a) and Azizi et al. (2016). These features are identified using plots of thermodynamic parameters, namely temperature, pressure, and hydrate saturation. Further, dissociation front is identified for each of the cases, and its transient variation is spatially tracked and mathematically fitted to an exponential function. An effort is made toward identifying a characteristic range of exponent for the different hydrate mechanisms, namely heat transfer, fluid flow, and dissociation. Further, we have also categorized the range of characteristic exponents along with their respective shapes (piston/non-piston/extended/stable) as well combination of mechanisms such as heat transfer + fluid flow, etc. In addition, energy conversion with respect to parametric analysis and quantitative analysis for each case is also performed to clearly infer the sensitivity toward maximizing hydrate dissociation.

Numerical modeling setup

In the present studies, a numerical has been developed for the purpose of numerical modeling the conceptualized hydrate reservoir. The framework can be used for numerical modeling of both field-scale and lab-scale experiments. The constituting model equations for the numerical framework are described as follows:

Model equations

I. Mass balance equation for methane (CH4)

$$\frac{\partial}{\partial t}\left(\varphi S_{Aq}\rho_{Aq}x_{Aq}^{m}+\varphi S_{G}\rho_{G}x_{G}^{m}\right)=\nabla.\left[-k\frac{k_{rAq}\rho_{Aq}}{\mu_{Aq}}x_{Aq}^{m}\left(\nabla P_{Aq}-\rho_{Aq}g\right)-k\left(1+\frac{b}{P_{G}}\right)\frac{k_{rG}\rho_{G}}{\mu_{G}}x_{G}^{m}\left(\nabla P_{G}-\rho_{G}g\right)\right]+q_{Aq}x_{Aq}^{m}+q_{G}x_{G}^{m}+\frac{M^{m}}{M^{h}}m_{H} \tag{1}$$

II. Mass balance equation for water (H_2O)

$$\frac{\partial}{\partial t}\left(\varphi S_{Aq}\rho_{Aq}x_{Aq}^{w}+\varphi S_{G}\rho_{G}x_{G}^{w}+\varphi S_{I}\rho_{I}\right)=\nabla.\left[-k\frac{k_{rAq}\rho_{Aq}}{\mu_{A}}x_{Aq}^{w}\left(\nabla P_{Aq}-\rho_{Aq}g\right)-k\left(1+\frac{b}{P_{G}}\right)\frac{k_{rG}\rho_{G}}{\mu_{G}}x_{G}^{w}(\nabla P_{G}-\rho_{G}g)\right]+q_{Aq}x_{Aq}^{w}+q_{G}x_{G}^{w}+\frac{q_{I}\rho_{Aq}}{LWH}+\frac{NM^{w}}{M^{h}}m_{H} \tag{2}$$

III. Mass balance equation for inhibitor

$$\frac{\partial}{\partial t}\left\{\left[\varphi S_{Aq}+(1-\varphi)\rho_{R}K_{d}^{i}\right]\rho_{R}x_{Aq}^{i}\right\}=\nabla.\left[-k\frac{k_{rAq}\rho_{Aq}}{\mu_{Aq}}x_{Aq}^{i}\left(\nabla P_{Aq}-\rho_{Aq}g\right)\right]+q_{Aq}x_{Aq}^{i} \tag{3}$$

IV. Mass balance equation for hydrate

$$\frac{d}{dt}\{\varphi S_{H}\rho_{H}\}=-\dot{m}_{H} \tag{4}$$

The rate of hydrate dissociation is determined using the kinetics described by the Kim-Bishnoi model proposed in 1987. The rate of hydrate dissociation $\left(\dot{m}_{H}\right)$ is expressed mathematically as

$$\dot{m}_{H}=-k_{0}F_{A}A\left(f_{eq}-f_{G}\right) \tag{5}$$

Here, k_0 denotes dissociation rate constant, F_A denotes area adjustment factor, A is the area taking part in the reaction, and f denotes fugacity of the gas phase.

Further, the dissociation rate constant (k_0) is expanded as

$$k_{0}=kd0.e^{\left(\frac{\Delta E_{a}}{RT}\right)} \tag{6}$$

where $kd0$ is the intrinsic hydration reaction constant and E_a denotes hydration activation energy.

V. Energy balance equation

$$\begin{aligned}&\frac{\partial}{\partial t}\left\{\begin{array}{c}(1-\varphi)\rho_{R}C_{R}T+\varphi S_{Aq}\rho_{Aq}\left[x_{Aq}^{w}u^{w}+x_{Aq}^{m}\left(u^{m}+u_{sol}^{m}\right)+x_{Aq}^{i}u_{sol}^{i}\right]+\varphi S_{G}\rho_{G}\left(x_{G}^{w}U_{G}^{w}+x_{G}^{m}U_{G}^{m}+U_{dep}\right)\\+\varphi S_{I}\rho_{I}u_{I}+\varphi S_{H}\rho_{H}u_{H}+\varphi\Delta S_{H}\rho_{H}\Delta H^{0}+\varphi\Delta S_{I}\rho_{I}\Delta H^{f}\end{array}\right\}\\&=\nabla.\{[(1-\varphi)K_{R}+\varphi S_{H}K_{H}+\varphi S_{I}K_{I}+\varphi S_{A}K_{A}+\varphi S_{G}K_{G}]\nabla T\}\\&+\nabla.\left[k\left(1+\frac{b}{P_{G}}\right)\frac{k_{rG}\rho_{G}}{\mu_{G}}(\nabla P_{G}-\rho_{G}g)\left(x_{G}^{w}h_{G}^{w}+x_{G}^{m}h_{G}^{m}+H_{dep}\right)+k\frac{k_{rAq}\rho_{Aq}}{\mu_{Aq}}\left(\nabla P_{Aq}-\rho_{Aq}g\right)\left(x_{Aq}^{w}h^{w}+x_{A}^{m}\left(H^{m}+H_{sol}^{m}\right)+x_{A}^{i}H_{sol}^{i}\right)\right]+\frac{q_{I}\rho_{Aq}h^{w}}{LWH}+\frac{q_{d}}{LWH}\\&+\left\{q_{G}\left[x_{G}^{w}h_{G}^{w}+x_{G}^{m}h_{G}^{m}+H_{dep}\right]+q_{Aq}\left[x_{Aq}^{w}h^{w}+x_{A}^{m}\left(H^{m}+H_{sol}^{m}\right)+x_{A}^{i}H_{sol}^{i}\right]\right\}\end{aligned} \tag{7}$$

Here, ρ_i, φ, S_i, and K_i represent density, porosity, saturation, and thermal conductivity of ith phase(methane, water, hydrate, and rock), respectively.

Numerical framework validation

To test the reliability of the developed numerical framework, experimental studies conducted by Yousif et al. (1991) are used as benchmark for validation. More specifically, experimental results of cumulative methane produced and transient position of dissociation front are validated against the numerical prediction of the model. Yousif et al. (1991) carried out experimental hydrate formation and dissociation on sandstone cores. In the present study, 1-D numerical model with Δx=0.3cm (grid size=50) was used for simulation. The relevant parameters used in the simulation are described in Table 1.

Table 1 Relevant simulation parameters used for experimental validation

S. No	Parameter	Value
1	Length of domain	15cm
2	Absolute permeability, md	100
3	Temperature, K	274
4	Initial pressure, MPa	3.17
5	Porosity, %	18.8
6	Initial hydrate saturation, %	42.76
7	Initial water saturation, %	17
8	Depressurization, P0(MPa)	2.495
9	ΔE/R (K)	9400

The rate constant was fitted to the experimental value with a value of k0= 2.4x10^4 (mol/m^2.Pa.Sec). As can be seen from Figures 1 and 2, the numerical predictions are fairly accurate with error, Ɛ, less than 2%. Hence, in view of the above validation, it is justified that the developed framework is reliable and capable of simulating hydrate dissociation behavior.

Case setup

As the dissociation of hydrate proceeds with time, the hydrate reservoir can be divided into two discrete zones. The first zone consists of dissociated hydrate; i.e., when complete dissociation of hydrate occurs, the hydrate saturation becomes zero (Sh=0), while the other zone consists of un-dissociated hydrate where hydrate saturation is essentially nonzero (Sh≠0). The un-dissociated hydrate zone may include different subzones where hydrate saturations are of different magnitudes (partially dissociated) and, essentially, nonzero. The interface where these two discrete zones meet is termed as the dissociation front.

For the present studies, a 1-D conceptual model of a hydrate reservoir having a length of 1.0m is considered. The realized model of hydrate reservoir is also shown (see Fig. 3). The production well for gas is located at *x*=0 (see Fig. 3). To ascertain an appropriate cell size for discretization, the grid independence test is carried out using dissociation front as the parameter.

Grid independence test

Before beginning any rigorous numerical study, it is essential to use a grid number that is sufficiently fine enough to capture the modeled phenomenon adequately. Generally, an appropriate grid number is selected when the value of a specific "quantifiable parameter" tends to be replicated (remains approximately the same) over several different grid sizes. In the present study, "hydrate dissociation front location" is chosen as the parameter for conducting the grid independence study. As mentioned above, for a domain length of 1m, mesh 1 (5 grids, Δx=0.2m), mesh 2 (10 grids, Δx=0.1m), mesh 3 (20 grids, Δx=0.05m), and mesh 4 (30 grids, Δx=0.033m) have been investigated for tracking dissociation front. The transient location (spatial 1D) of dissociation front is depicted below.

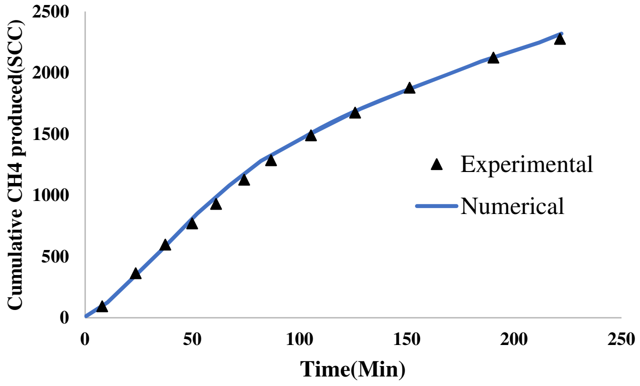

Fig. 1 Cumulative methane produced during depressurization (Yousif et al. 1991)

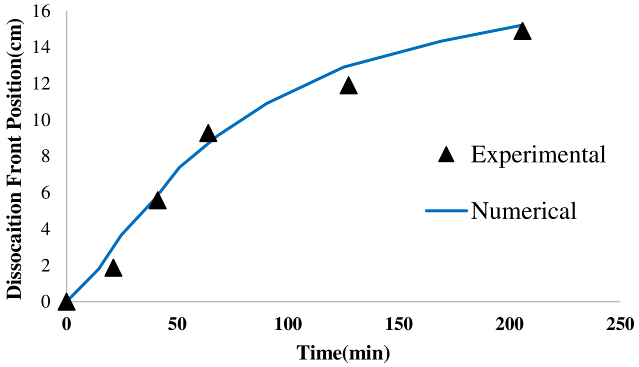

Fig. 2 Transient evolution of dissociation front during depressurization (Yousif et al. 1991)

As shown in Figure 4, grid size 5 shows a rough estimation of the tracked dissociation front. When the grid size is increased to 10, the dissociation front shows a much more accurate and refined behavior. However, halfway between the domain length, x/L=0.5, the dissociation front shows deviation from the previously overlapping curves. When the grid size is increased to 20, the initial behavior is replicated, and the further behavior of dissociation front is refined. In order to confirm that grid size 20 is capable of simulating the behavior accurately, a grid size of 30 was also used for simulation. As

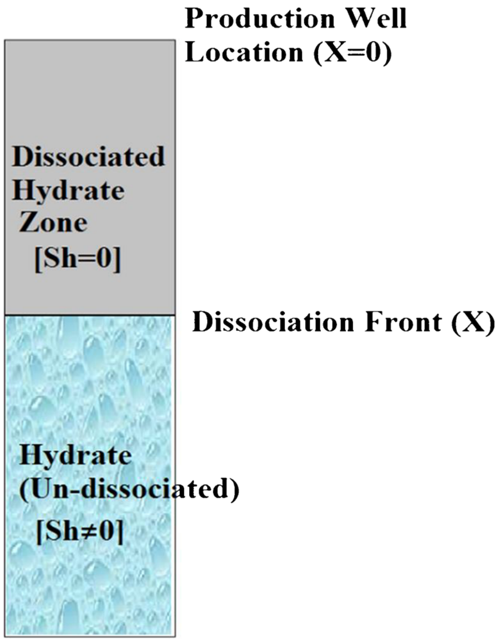

Fig. 3 Illustration of conceptualized hydrate reservoir model with production well, dissociation front position, and hydrate zones.

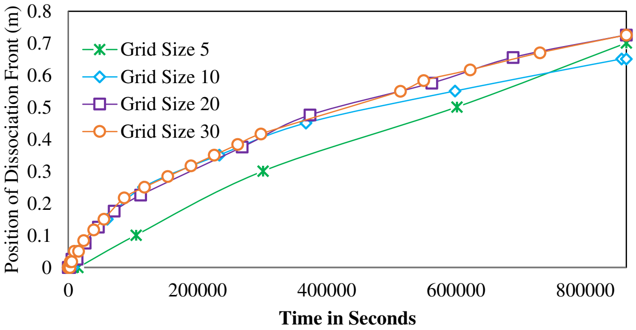

Fig. 4 Grid independence test: spatial location of dissociation front for the base case (#B) for different grid sizes

can be noted from the figure (see Fig. 4), the dissociation front shows an overlapping behavior for both grid size 20 and grid size 30. Hence, in light of the above discussion, grid size 20 is chosen as the appropriate grid size for conducting further numerical simulation in this study.

Simulated case matrix

The different hydrate dissociation mechanisms like heat transfer, flow-controlled, and hydrate dissociation are investigated in the present study. The present study is based on the sandstone hydrate reservoirs. More specifically, the parameters used are based on sandstone reservoirs discovered in the Nankai Trough (Takano et al. 2009), at a depth of 1100–1250m. The overall dissociation mechanism is actually a complex function of different parameters like overall thermal conductivity (K), intrinsic permeability (k), wellbore heating temperature (T_b), bottom hole pressure (P_b), and rate constant (k_{d0}). Here, it must be noted that K represents thermal conductivity under (liquid) saturated conditions. The intrinsic permeability of porous media is measured prior to the hydrate formation. For the base case, the values are thermal conductivity (K=3.1W/m.K), intrinsic permeability (k=2.96x10^{-14}), wellbore heating temperature (T_b=278.15K), bottom hole pressure (P_b=2.7MPa), and rate constant (k_{d0}=3x10^4 mol/m^2.Pa.Sec).

The case matrix has been designed with a view to investigate these influencing parameters outlined in the literature. In total, 20 cases have been simulated to clearly delineate the role of these parameters in determining the dissociation behavior.

Results and discussion

The cases designed in Table 2 are simulated to ascertain the extent of their influence in determining the hydrate dissociation behavior. The Results and discussion section has been divided into three subsections to allow better understanding and smooth transition into the advancing stage of inferring results. These subsections entail discussions on (i) quantitative analysis and energy conversion and (ii) thermodynamic parameters, namely pressure, temperature, and mathematical fitting for determining characteristics of DF, i.e., piston-/non-piston-type front. The final section (iii) is based on deciphering the mechanisms associated with each of these cases. To better assess the impact of each parameter, a base case (indented B) in Table 2 is taken as a reference.

Energy conversion and quantitative analysis

To evaluate the influence of different techniques and parameters, quantitative analysis, i.e., gas produced (Kg or m3), is necessary. Moreover, the extent of hydrate dissociated directly amounts to energy conversion. For clarity, plots of CH4 produced vs. time and hydrate converted to energy are depicted in Fig. 5.

Wellbore heating

As shown in Fig. 5., wellbore heating influences the cumulative mass of CH4 produced. With increasing wellbore temperature, the initial rate of CH4 production remains nearly the same. However, with slow heat diffusion within the reservoir, cumulative CH4 produced doubles during the latter period. The energy conversion from hydrate can be inferred from the bar chart. As can be noted, energy conversion shows a directly proportional relationship with temperature. From a low value of 52% for case a1, the conversion efficiency increases to 64% for case a2 and 94% for case a3, and 100% dissociation of hydrate and subsequent conversion to energy is observed for case a4.

Intrinsic rate constant

For intrinsic rate constant, as can be noted from CH4 time plot, for case e1 with a low intrinsic rate constant, the cumulative mass of CH4 produced reaches around 16Kg. For case e2, a reduced intrinsic rate constant by a factor of 10 does not appreciably reduce the cumulative mass of CH4 produced. Similar behavior is observed for cases e3 and e4, respectively. Overall, the net production curves for cases e1, e2, e3, and e4 show close proximity, which implies that changing intrinsic constant hardly affects the net production. A similar trend is observed in energy conversion where hydrate dissociation and its subsequent conversion essentially remain in close proximity of 80%. Therefore, it is inferred that the sensitivity of the intrinsic rate constant is relatively low when it comes to influencing the cumulative production of methane gas from hydrate reservoirs.

Table 2 Different cases with respective values

Case no.	Rate constant k_{d0} $\frac{mol}{m^2.Pa.s}$	Intrinsic Permeability k (m^2)	Thermal conductivity K (W/m.K)	Wellbore heating temp. T_b (K)	Bottom hole pressure P_b (MPa)	Initial conditions
Base (B)	$3x10^{4}$	$2.96x10^{-14}$	3.1	**278.15**	2.7	Sg=0 Sw=0.5
a1	$3x10^{4}$	$2.96x10^{-14}$	3.1	**274.25**	2.7	Sg=0 Sw=0.5
a2	$3x10^{4}$	$2.96x10^{-14}$	3.1	**275.3**	2.7	Sg=0 Sw=0.5
a3	$3x10^{4}$	$2.96x10^{-14}$	3.1	**280.15**	2.7	Sg=0 Sw=0.5
a4	$3x10^{4}$	$2.96x10^{-14}$	3.1	**281.65**	2.7	Sg=0 Sw=0.5
b1	$3x10^{4}$	$2.96x10^{-14}$	**1.1**	278.15	2.7	Sg=0 Sw=0.5
b2	$3x10^{4}$	$2.96x10^{-14}$	**2.1**	278.15	2.7	Sg=0 Sw=0.5
b3	$3x10^{4}$	$2.96x10^{-14}$	**6.1**	278.15	2.7	Sg=0 Sw=0.5
b4	$3x10^{4}$	$2.96x10^{-14}$	**9.1**	278.15	2.7	Sg=0 Sw=0.5
c1	$3x10^{4}$	$2.96x10^{-14}$	3.1	278.15	**4**	Sg=0 Sw=0.5
c2	$3x10^{4}$	$2.96x10^{-14}$	3.1	278.15	**3**	Sg=0 Sw=0.5
c3	$3x10^{4}$	$2.96x10^{-14}$	3.1	278.15	**2**	Sg=0 Sw=0.5
c4	$3x10^{4}$	$2.96x10^{-14}$	3.1	278.15	**1**	Sg=0 Sw=0.5
d1	$3x10^{4}$	**$2.96x10^{-12}$**	3.1	278.15	2.7	Sg=0 Sw=0.5
d2	$3x10^{4}$	**$2.96x10^{-13}$**	3.1	278.15	2.7	Sg=0 Sw=0.5
d3	$3x10^{4}$	**$2.96x10^{-15}$**	3.1	278.15	2.7	Sg=0 Sw=0.5
d4	$3x10^{4}$	**$2.96x10^{-16}$**	3.1	278.15	2.7	Sg=0 Sw=0.5
e1	**$3x10^{2}$**	$2.96x10^{-14}$	3.1	278.15	2.7	Sg=0 Sw=0.5
e2	**$3x10^{3}$**	$2.96x10^{-14}$	3.1	278.15	2.7	Sg=0 Sw=0.5
e3	**$3x10^{5}$**	$2.96x10^{-14}$	3.1	278.15	2.7	Sg=0 Sw=0.5
e4	**$3x10^{6}$**	$2.96x10^{-14}$	3.1	278.15	2.7	Sg=0 Sw=0.5

The bold values indicate the changed values of parameters for each of the case index, i.e. a, b, c, d, and e, respectively

Intrinsic permeability

In case of intrinsic permeability, a much more diverse trend is observed regarding the cumulative production of methane. Contrary to expectation, high intrinsic permeability case d1 shows a much lower cumulative methane production than that of the base case. This occurs due to a high magnitude of differential pressure, ΔP. A detailed explanation is given in the next section, where thermodynamic parameters are discussed. For cases d2 and d3 with a much-reduced permeability, the production curve follows the base case. However, a much-reduced permeability restricts the flow of gas and pushes the hydrate into the stability zone. The energy conversion from hydrate roughly reached up to 80% for cases d2 and

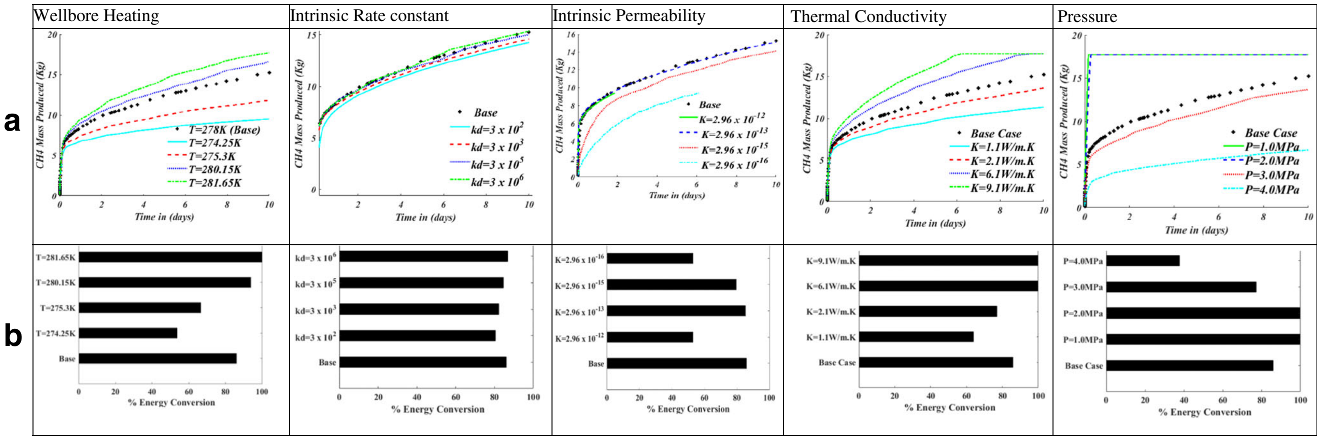

Fig. 5 (**a**) Mass of CH4 produced and (**b**) energy conversion from hydrate (%). Wellbore heating: cases a1, a2, a3, and a4. Overall thermal conductivity: cases b1, b2, b3, and b4. Depressurization: cases c1, c2, c3, and c4. Intrinsic permeability: cases d1, d2, d3, and d4. Intrinsic rate constant: cases e1, e2, e3, and e4

d3, whereas in cases d1 and d4, only 52% conversion is achieved.

Thermal conductivity

The effect of thermal conductivity is studied in cases b1, b2, b3, and b4. From the cumulative gas production plot, it can be noted that complete hydrate dissociation occurs for case b4 and the resulting production curve reaches a saturation value. A similar trend is observed for case b3 as well, where CH4 production reaches the maximum value and touches the saturation limit. Moreover, the overall line plot of CH4 shows a much wider distribution, which implies that thermal conductivity indeed plays a crucial role in determining the dissociation behavior. The energy conversion from hydrate shows an increasing trend with increasing thermal conductivity. For the base case, the energy conversion efficiency is found to be 80%, while for much lower thermal conductivity than the base case, energy conversion efficiencies of 63% and 78% are observed. On the other hand, a higher thermal conductivity than the base case promotes heat dissociation within the sediments, promoting thermal stimulation, and subsequent complete dissociation of hydrate is observed, i.e., 100% hydrate dissociation to release methane.

Depressurization

Depressurization is investigated through 4 different cases c1, c2, c3, and c4, respectively. Here, the driving force is the differential pressure, and the different cases are designed to provide magnitudes that are relatively large and relatively low. As can be noted from Table 2, cases c3 and c4 have a large driving force for depressurization. While cases c1 and c2 have a much smaller driving force, it is evident from Fig. 5 that the increasing depressurizing leads to the rapid dissociation of hydrate. Notice the almost vertical lines from cumulative CH4 production from the line plot indicating that hydrate dissociates rapidly and, consequently, reaches a saturation limit indicated by the horizontal line. The same trend is observed for cases c2 and c3. For cases, c1 and c2, a much more gradual release of methane occurs. The cumulative methane produced for cases c1 and c2 is lower than that of the base case for the runtime of 10 days' period. The energy conversion from hydrate for cases c3 and c4 is found to be 100% due to complete dissociation of hydrate. However, for cases c1 and c2, the energy conversion from hydrate is found to be 40% and 78%, respectively.

Characteristics of dissociation front, thermodynamic pressure, and temperature

In order to deduce the mechanisms governing the dissociation of hydrate for different cases, it is imperative to analyze the thermodynamic parameters. For his study, thermodynamic parameters like pressure distribution within the reservoir, equilibrium pressure calculated using the temperature distribution, and spatial hydrate saturation distribution have been plotted and investigated for each case.

The characteristic features of the dissociation front are determined using a sensible and practical criterion of fitting exponent. The classification is based on the exponent value, which varies between 0 to 0.5 and 0.5 to 1 (see Fig. 6b). This criterion, in combination with advancing characteristics of spatial hydrate saturation plot, provides relevant information for this purpose. Further, here, the advancing features of spatial hydrate saturation plot are classified as piston type, stable non-piston type, and extended non-piston type, depending upon the shape of the hydrate saturation plot.

Base case description

In the base case, as shown in Fig. 6a, the spatial saturation plot shows a sharp cusp at the point of transition. This shape of the

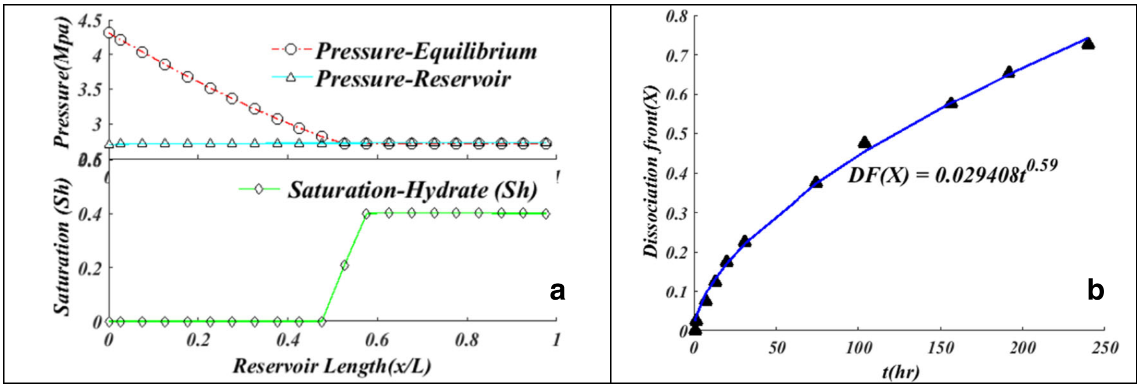

Fig. 6 **a** Spatial variation of reservoir and equilibrium pressure along with hydrate saturation for the base case. **b** Advancing characteristics with fitting exponent

curve is referred to as the piston type. Such behavior indicates that hydrate saturation behaves in a similar way as that of a piston. In terms of hydrate dissociation, it means that hydrate dissociation is limited to a small region. This small region demarcates the zone of fully dissociated hydrate and non-dissociated hydrate. In another way, it implies that the dissociation front range is relatively narrow, and a sharp dissociation front is formed.

Referring to Fig. 6b, the fitting exponent is found to be 0.59, which is in close proximity to 0.5. Moreover, as shown in Fig. 6a, the reservoir pressure decreases to the bottom hole pressure throughout the grid, which implies that fluid flow does not play a major role. It can also be noticed that equilibrium pressure shows a rapid transition from its initial value of 4.3MPa to, finally, where it nearly overlaps with the reservoir pressure. Moreover, the foot of the piston, i.e., dissociation curve, coincides with the spatial position where equilibrium pressure approximately becomes equal to the reservoir pressure. Therefore, it can be concluded that heat transfer plays the governing role in the base case.

Effect of different wellbore heating temperatures

For the wellbore heating cases, a1, a2, a3, and a4, the figures are depicted in Fig. 7. As mentioned earlier, subfigures a and b illustrate the variation of pressure within the reservoir and equilibrium pressure followed by the evolution of hydrate saturation within the reservoir. The latter figure, i.e., subfigure b, depicts the fitting of dissociation front in order to determine the range of exponent and consequentially decipher and attribute the associated mechanism with each case. To avoid confusion within the 4×2 matrix of figures, each case has been labeled below with its respective value.

From Fig. 7a, for case a1, it is evident that the evolution curve of hydrate saturation depicts a gradual transition between the dissociated and un-dissociated hydrate zone. As hydrate dissociation extends over a single grid, such a dissociation front is relatively narrow and is termed as a stable non-piston type. Additionally, in the same Fig. 7a, the pressure within the reservoir along with equilibrium pressure shows a distinct behavior. More precisely, the pressure distribution within the reservoir is much higher than the equilibrium pressure within the hydrate zone. This essentially means that fluid flow is the dominant mechanism that governs the behavior of this system. Moreover, it can be estimated that during the late dissociation stage, where reservoir and equilibrium pressure overlap, heat transfer will play a key role in determining further dissociation behavior. Hence, overall, it can be stated that fluid flow and heat transfer are the controlling mechanisms characterized by a high exponent value of 0.75.

For case a2, the pressures and the saturation curves depict similar inherent characteristics as those for previous case a1. However, unlike case a1, where the reservoir pressure curves and equilibrium pressure curves are distinctly separated from each other, these curves for case a2 depict a much closer approach toward each other. Reduced heat transfer plays a vital role along with fluid flow in controlling the dissociation within the reservoir. This essentially implies that, comparatively, heat transfer plays a far more dominant role in case a2. Additionally, the saturation curve exhibits the same stable non-piston-type characteristics. Hence, controlling mechanisms for case a2 are stated as heat transfer and fluid flow with an exponent of 0.57.

For case a3, it must be noticed from the saturation curve that hydrate dissociation extends to two distinct grids. Also, it can be seen that there is a gradual transition from the dissociation zone to the hydrate zone. Such type of characteristic saturation curve is inferred as extended non-piston-type dissociation front. It means that the dissociation zone extends to a much larger zone in comparison to previous cases a1 and a2. Next, the pressure curves show strong overlapping trends, which means that there is a limited heat supply. As such, the overall controlling mechanism is governed by dissociation and heat transfer, respectively.

For case a4, similar inherent characteristics as that of case a3 are observed, which are attributed to the same mechanisms,

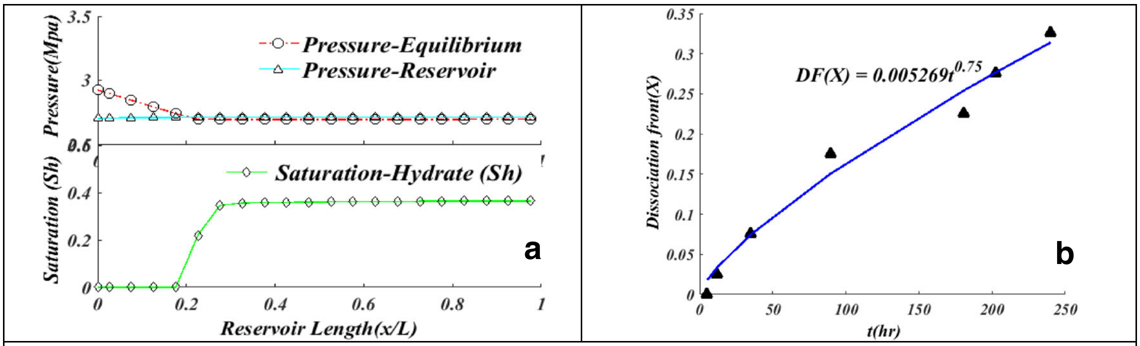

Case a1: $T = 274.25K$

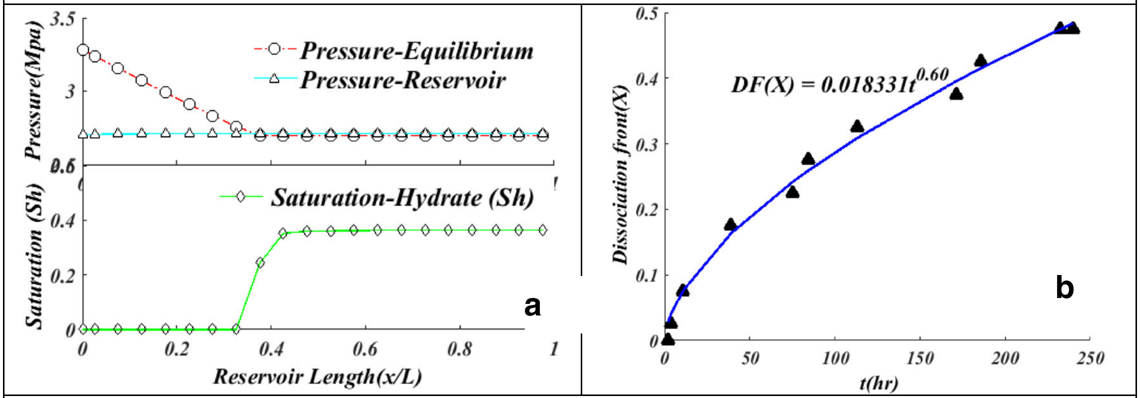

Case a2: $T = 275.3\text{K}$

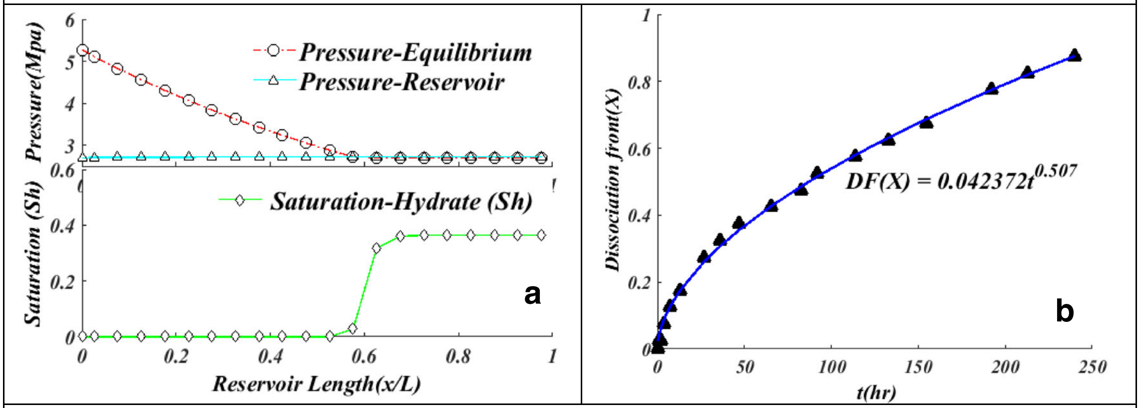

Case a3: $T = 280.15K$

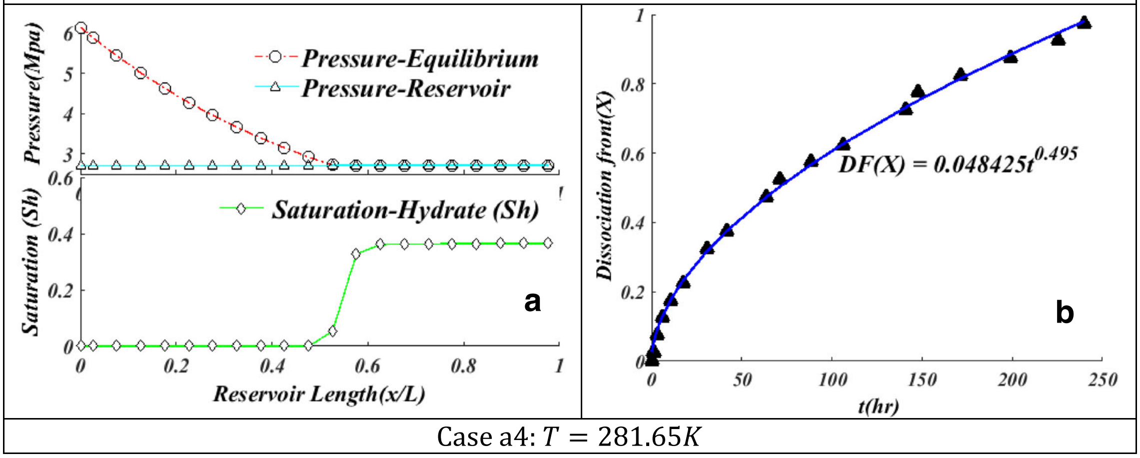

Case a4: $T = 281.65K$

Fig. 7 **a** Spatial variation of reservoir and equilibrium pressure along with hydrate saturation for cases a1 and a2. **b** Advancing characteristics with fitting exponent i.e., dissociation and heat transfer with characteristic exponent value near 0.5.

Effect of varying overall thermal conductivity

The effect of thermal conductivity is investigated using cases b1, b2, b3, and b4 (see Table 2). The plots of thermodynamic parameters, namely, reservoir, equilibrium pressure, and saturation progression, are depicted in Fig. 8.

For case b1, from Fig. 8a, it can be seen that the saturation curve exhibits dissociation, which extends over a single grid, which is termed as stable non-piston-type dissociation front. Moreover, the equilibrium and reservoir pressure curves show close proximity, which implies that both fluid flow and heat transfer are relevant mechanisms for this case. These combined controlling mechanisms are exhibited by a characteristic exponent value of 0.60.

In case b2, similar patterns are observed for both plots of hydrate saturation and pressure. The closely approaching pressure curves indicate limited heat transfer. Moreover, a close analysis of pressure values indicates that the system behavior approaches more toward being controlled by heat transfer, in comparison to the magnitude of governance through fluid flow. However, overall for case b2, the characteristic curves of the system confirm that both heat transfer and fluid flow are relevant with a characteristic exponent of 0.57.

With a further increase in thermal conductivity of sediments, we arrive at the base case. Recalling from the previous section, the controlling mechanism for the base case is found to be heat transfer only. This is in accordance with our analysis and understanding of the previous case, which indicates that the system approaches more toward being governed through heat transfer only.

For case b3, we have a much higher thermal conductivity than the base case. The shape of the saturation curve (see Fig. 8a) indicates that the dissociation zone extends over two grid nodes, which indicates that the dissociation front extends over a range rather than a sharp one. Hence, as aforementioned in the previous sections, the dissociation front is categorized as an extended non-piston type. The pressure curves from Fig. 8a show an overlapping trend, which indicates limited heat transfer. Additionally, it can be noticed from Fig. 8a that the point of overlapping of reservoir and equilibrium pressures does not match the foot coordinate of dissociated hydrate zone (refer to saturation curve). Therefore, it means that dissociation is the controlling mechanism along with heat transfer. The behavior of the system is characterized by an exponent value of 0.51.

For case b4, we again observe similar patterns for saturation and pressure curves. Hence, it is reasonable to conclude that controlling mechanisms for this case are the same, i.e. dissociation combined with heat transfer. The relative magnitudes for these mechanisms definitely tend to be somewhat comparable because of the shape of the dissociation curve (inferred from saturation plot). This is because the saturation curve shows a plateau formation. In case of dissociation mechanism domination, the dissociation curve shows a far flatter curve that rises much more gradually over an extended part of the domain. Hence, in such a scenario, the dissociation mechanism is stated to be more dominating than its counterpart, i.e., whether heat transfer or fluid flow. Such a case is discussed in the upcoming section.

Effect of different depressurization magnitudes

Depressurization is studied in cases c1, c2, c3, and c4. The plots of thermodynamic parameters are depicted in Fig. 9. Like previous sections, Fig. 9a and Fig. 9b describes the pressure, saturation, and mathematical fitting for characteristic exponent for each of these cases.

Case c1 describes a scenario where a small magnitude of depressurization is given as a perturbation to the system in order to move the system toward instability or “out of gas hydrate stability conditions (P, T).” Since initial temperature of the reservoir is 278.15K, the equilibrium pressure turns out to be approximately 4.3MPa. The depressurization for c1 is carried out using a pressure of 4MPa. The response of the reservoir is depicted in Fig. 9a, which indicates that pressure drops throughout the reservoir to approximately bottom hole pressure, i.e., 4MPa. The close approaching pressure curves indicate that the limited heat transfer mechanism alone determines the pace of hydrate dissociation. As can be seen, the dissociation zone is very narrow (see Fig. 9a), and the hydrate saturation curve indicates that the progressing dissociation front follows a piston-like dissociation.

For case c2, the increased depressurization magnitude is reflected in a more extended depressurization throughout the hydrate reservoir. As reported in Fig. 9a, the saturation curve shows a more subtle dissociation, which is classified as a stable non-piston-type dissociation front. The pressure curves show a similar closely approaching trend. However, the detailed values indicate that heat transfer and fluid flow are the contributing mechanisms for the present case.

In case c3, as can be seen from Fig. 9a, an interesting dissociation pattern is revealed. Notice how the equilibrium pressure curve tends to saturate at a certain intermediate value between 2 and 3MPa. It essentially means that the temperature within the hydrate reservoir becomes constant. Therefore, the driving force is only due to pressure. The pressure difference is the only driving force for sustaining hydrate dissociation. It is also observed that hydrate saturation reduces within the extended part of the domain, which is inferred as an extended non-piston-like dissociation front. Moreover, toward the latter end of the reservoir, hydrate dissociation is more controlled due to limited heat transfer. Hence, it can be inferred that dominant mechanisms for case c3 are dissociation and heat

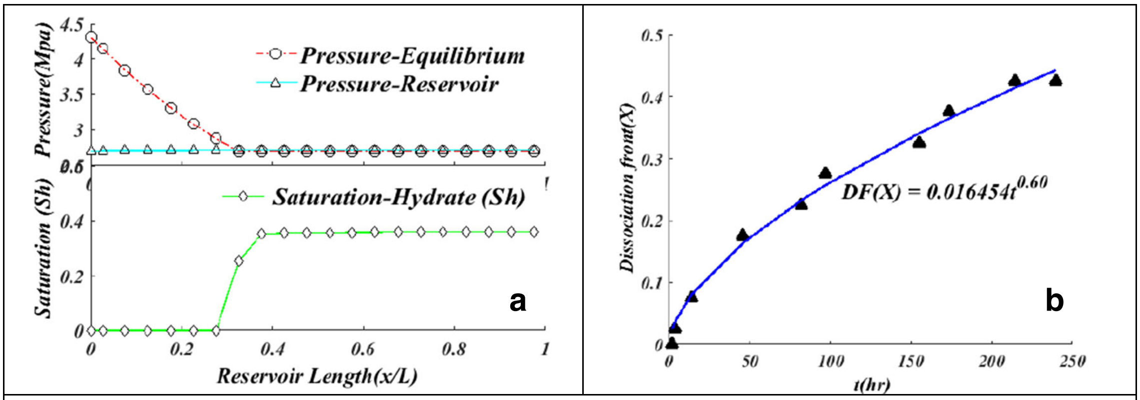

Case b1: $Kth = 1.1W/m.K$

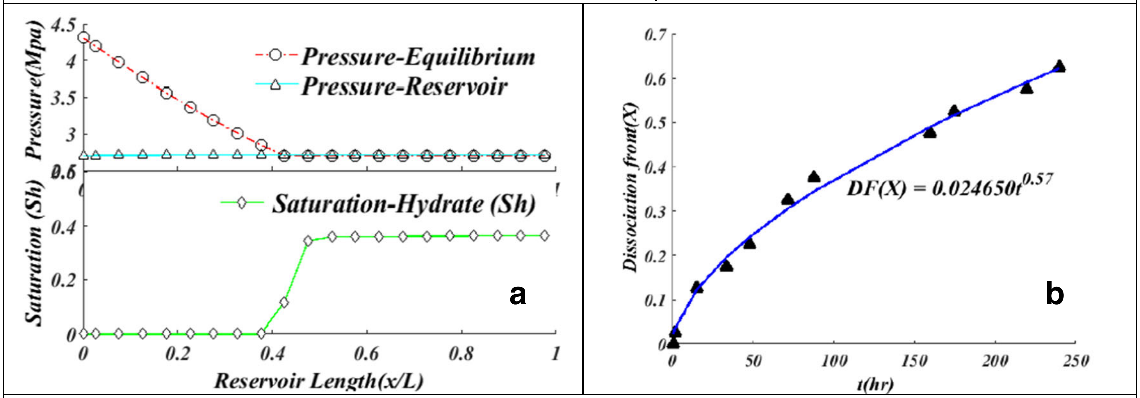

Case b2: $Kth = 2.1W/m.K$

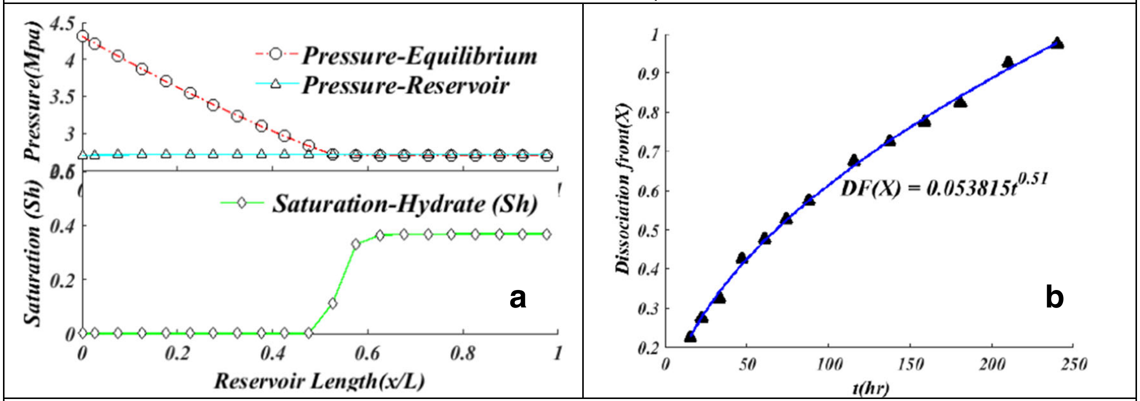

Case b3: $Kth = 6.1W/m.K$

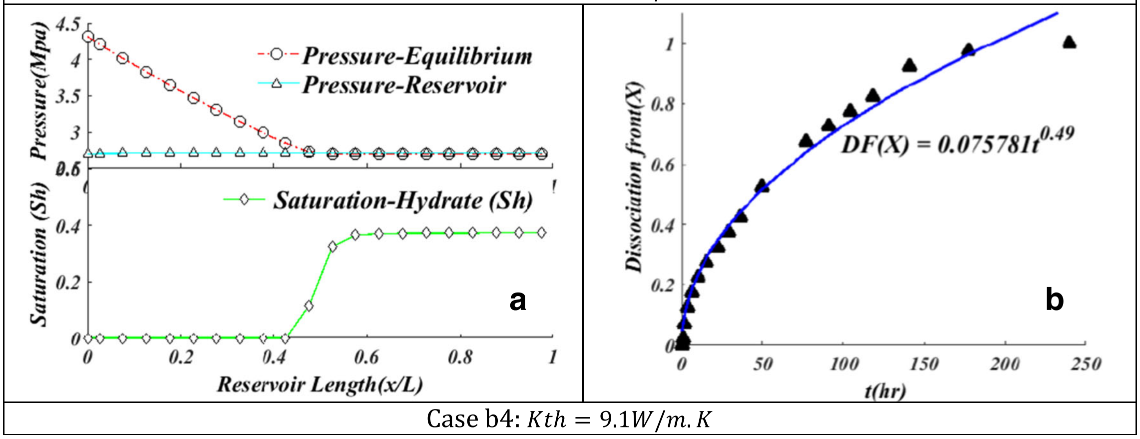

Case b4: $Kth = 9.1W/m.K$

Fig. 8 **a** Spatial variation of reservoir and equilibrium pressure along with hydrate saturation for cases b1 and b2. **b** Advancing characteristics with fitting exponent

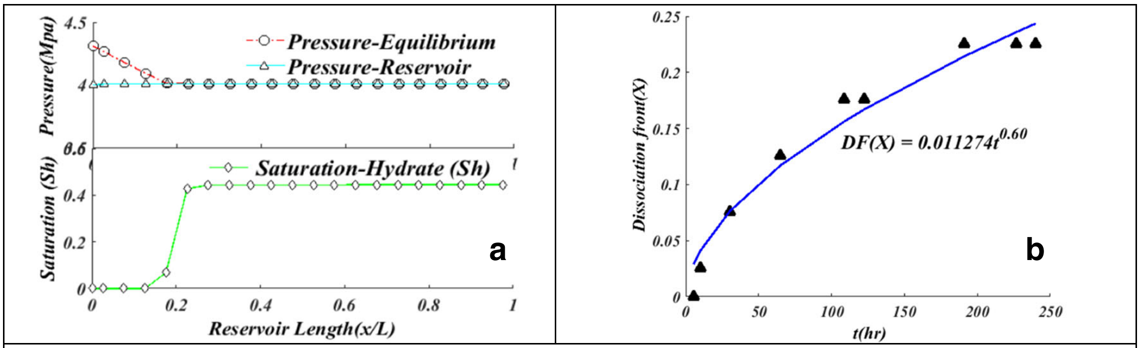

Case c1: $P = 4MPa$

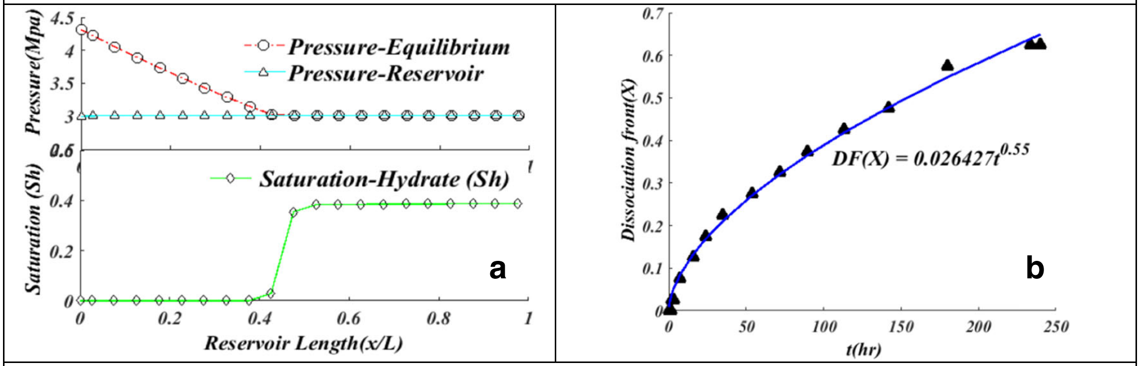

Case c2: $P = 3MPa$

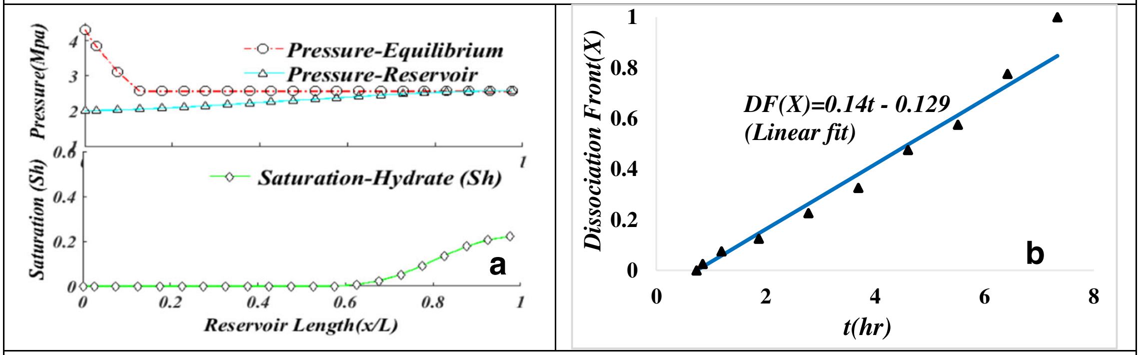

Case c3: $P = 2MPa$

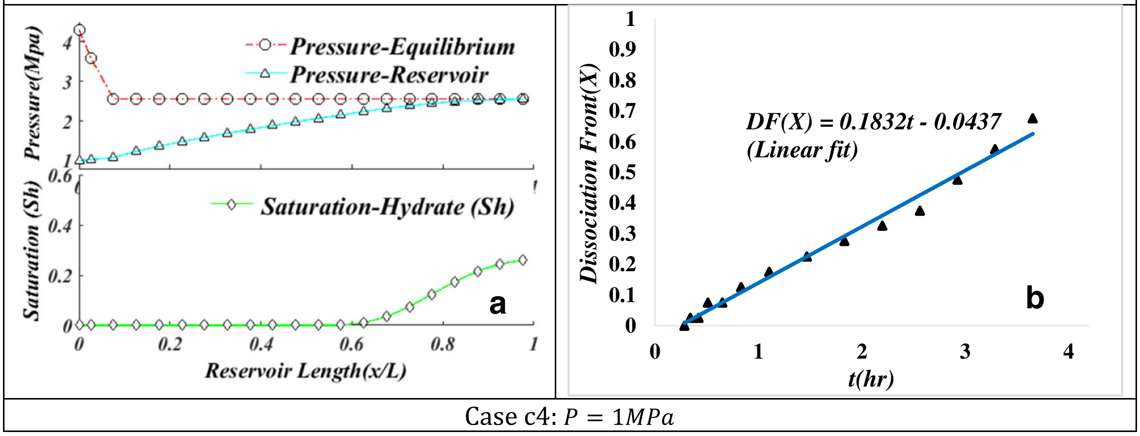

Case c4: $P = 1MPa$

Fig. 9 **a** Spatial variation of reservoir and equilibrium pressure along with hydrate saturation for cases c1 and c2. **b** Advancing characteristics with fitting exponent

transfer. A similar discussion and arguments can be presented for case c4. Here also, the same characteristics as the previous case are observed. Hence, the dominant mechanisms for case c4 are attributed to dissociation and heat transfer.

Effect of different intrinsic permeability

The impact of different intrinsic permeability is studied in cases d1, d2, d3, and d4. For case d1, we have considerably high permeability. As can be noticed from the plots (see Fig. 10a, case d1), the dissociation front can be seen to be extended over several grid points. This indicates that an extended non-piston dissociation front is present. A closer look (not shown here) indicates that equilibrium and reservoir pressure maintain close proximity to each other but do not overlap. Amalgamating the above two observations indicates that dissociation and fluid flow are the key mechanisms for case d1. The dissociation front shows a characteristic exponent value of 1 (linear fitting).

For case d2, with permeability reduced by a factor of 10, we see a much tighter progression of dissociation front. This is reflected in a much narrower dissociation front depicted in Fig. 10a for case d2. The saturation curve forms a typical extended non-piston-type shape. The pressure curves of equilibrium and reservoir tend to overlap each other, indicating that only heat transfer limits the hydrate dissociation among heat transfer and fluid flow. Overall, the key mechanisms for case d2 are heat transfer and dissociation. Moreover, the characteristic exponent for case d2 is found to be 0.57.

For case d3, the permeability is further reduced by a factor in comparison to case d2. As a result, the dissociation zone narrows down further. Unlike the previous case d2, we see that the dissociation front extends to only two grids. This is classified as a stable non-piston-type dissociation front. Moreover, it is noticeable from Fig. 10a that the pressure and saturation curves show consistency in the overlapping of pressures curves, and the point where hydrate saturation becomes nonzero. This means that heat transfer actually limits the dissociation. Hence, its inferred from the shape of the saturation curve and overlapping of pressure curves that heat transfer and dissociation are the active mechanisms for case d3. In terms of magnitude, unlike previous case d2, heat transfer dominates the dissociation mechanism.

Case d4 illustrates a classic case of how the hydrate dissociation mechanisms switch from one combination to another. Moreover, the transition from twin mechanisms to a single most dominant mechanism is also described in this case. As can be observed from Fig. 10a, unlike the previous three cases, the pressure curves show an increasing trend for this case (d4). This is expected because decreased permeability restricts the flow of gas within the reservoir. Hence, the pressure within the reservoir increases at the point where equilibrium and pressure curves meet. Beyond this point, the pressure increases, which implies that "secondary hydrate formation takes place." These localized pressure zones shift the equilibrium, which pushes the hydrate into the stability zone. In this scenario, limited heat transfer accounts for determining the dissociation behavior of hydrate within the reservoir. Moreover, as shown in Fig. 10a saturation curve, a spike in hydrate formation confirms our inference from pressure curves. The shape of the saturation curve indicates that a piston-like dissociation occurs within the reservoir.

Effect of varying intrinsic rate constant

The impact of the intrinsic rate constant is investigated in cases e1, e2, e3, and e4. In case e1, with a relatively low value intrinsic hydration rate constant, it is observed that the saturation plot depicts a dissociation front, which is extended over several grid indices (see case e1: Fig. 11a). The dissociation front shows a linear fitting, which implies dissociation occurs at a uniform rate within the reservoir. Moreover, it is observed that pressure curves of equilibrium and reservoir tend to asymptotically approach each other, indicating that fluid flow and dissociation play a key role in determining the extent of dissociation within the reservoir. The fitting of dissociation front yields the characteristic exponent value of 1 (linear fit).

In case e2, with higher intrinsic hydration constant, the dissociation front assumes a more of a parabolic shape (see case e2: Fig. 11b). This indicates that during the initial stage of dissociation, the rate of dissociation is relatively high. However, during the latter stage, the dissociation along with heat transfer determines the dissociation pattern. Another indication confirms that the above understanding can be seen from the shape of the saturation curve. As can be observed from Fig. 11a, the dissociation zone can be seen to extend over a couple of grids. This is in accordance with our inference from the pressure curves and dissociation front plot. As such, the saturation plot is classified as a stable non-piston type with a characteristic exponent value of 0.59.

For case e3, as can be noticed from the saturation plot, the dissociation zone is limited to a small portion of the domain. This indicates that dissociation proceeds in discrete portions completely before moving in deeper within the reservoir. Hence, it is inferred that a piston-like dissociation front is formed. The pressure and equilibrium curves coincide with each other, which implies heat transfer limits dissociation progression within the reservoir. Moreover, as can be noticed in the base case, a similar exponent value is obtained for the dissociation front governed through similar dissociation mechanisms.

For case e4, a much higher value of intrinsic hydration rate constant, i.e., 100 times the base case, is considered. However, as can be noticed by comparing the base case figures (Fig. 6a and b) and case e3 (Fig. 11a and b) with case e4, no major changes in inherent characteristics can be inferred. Hence, it's concluded that a piston-like dissociation front, along with heat transfer, is the characteristic feature and mechanism for case e4.

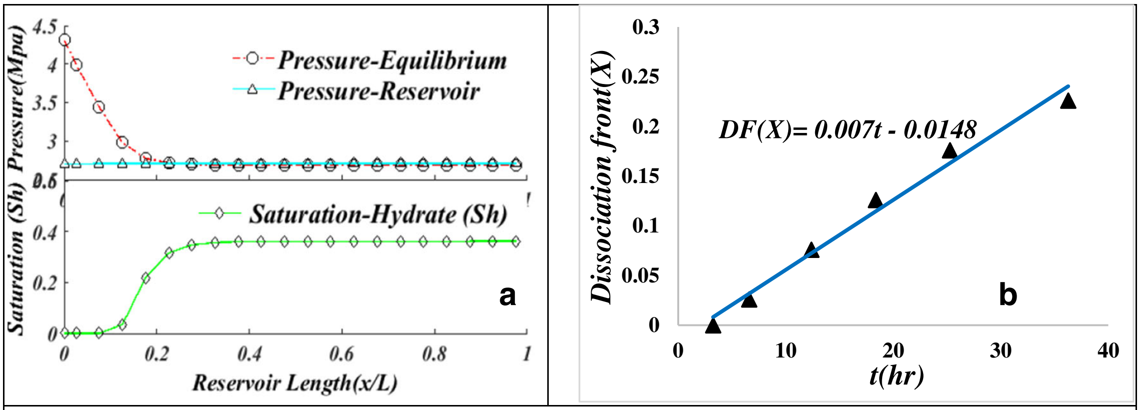

Case d1: $K = 2.96 \times 10^{-12}$

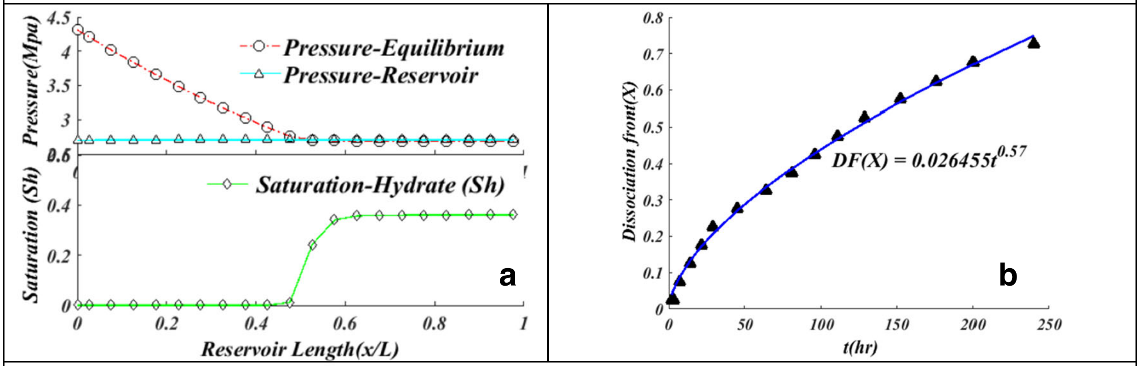

Case d2: $K = 2.96 \times 10^{-13}$

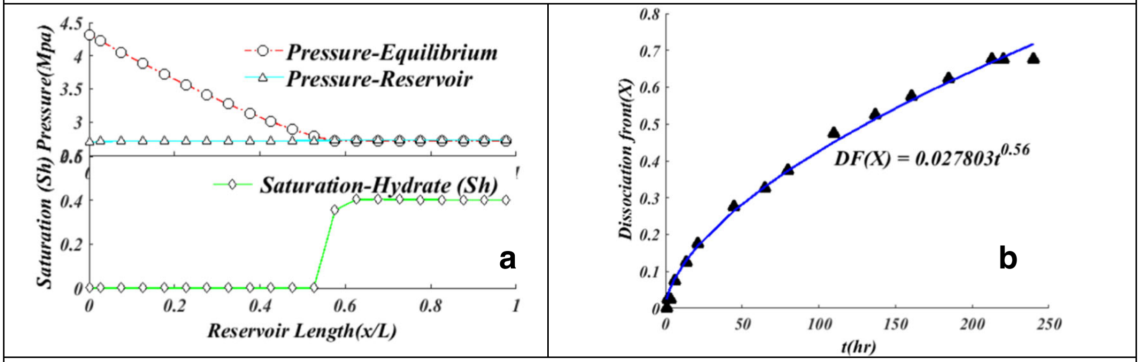

Case d3: $K = 2.96 \times 10^{-15}$

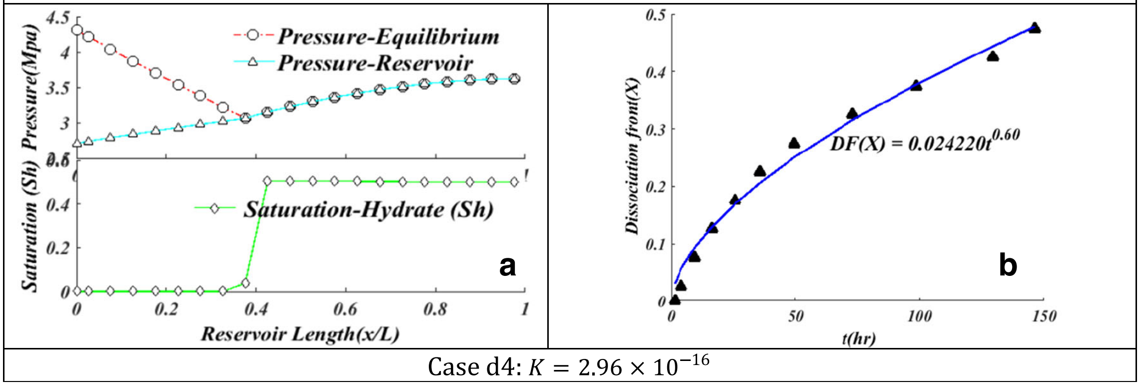

Case d4: $K = 2.96 \times 10^{-16}$

Fig. 10 **a** Spatial variation of reservoir and equilibrium pressure along with hydrate saturation for cases d1 and d2. **b** Advancing characteristics with fitting exponent

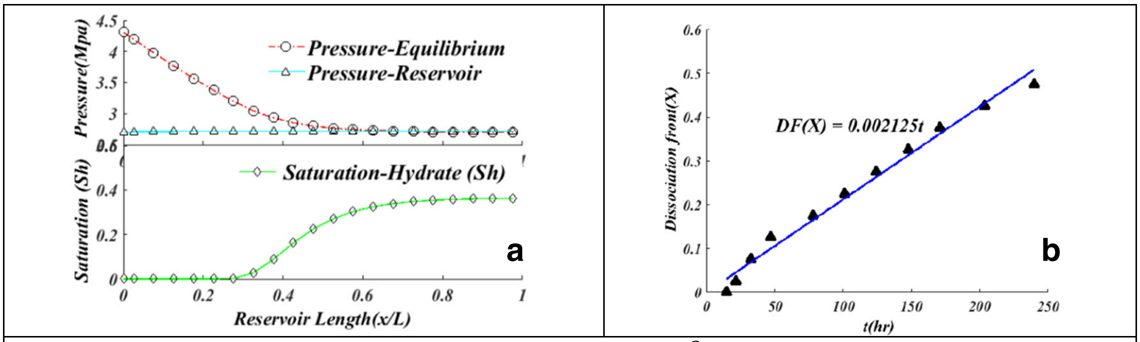

Case e1: $kd0 = 3 \times 10^2$

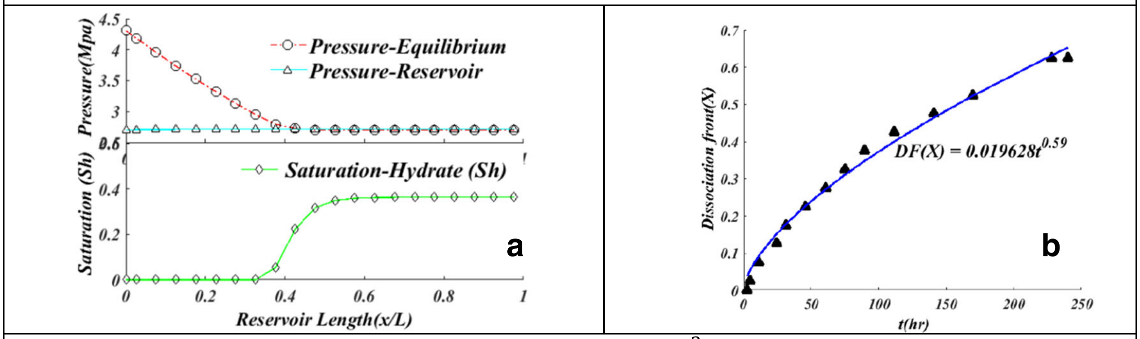

Case e2: $kd0 = 3 \times 10^3$

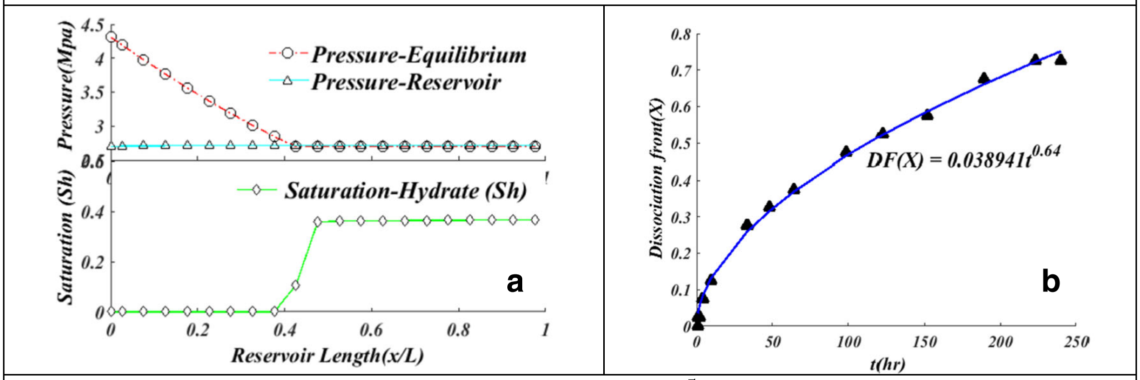

Case e3: $kd0 = 3 \times 10^5$

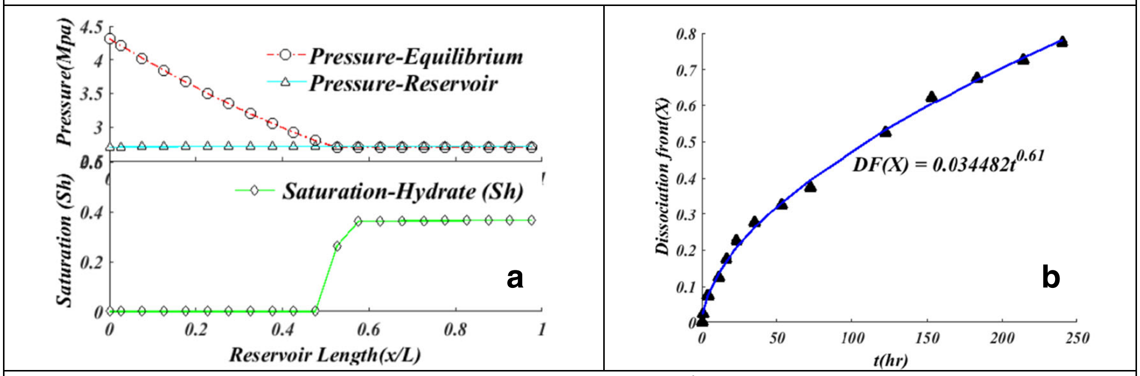

Case e4: $kd0 = 3 \times 10^6$

Fig. 11 **a** Spatial variation of reservoir and equilibrium pressure along with hydrate saturation for cases e1 and e2. **b** Advancing characteristics with fitting exponent

Dissociation mechanisms of hydrate (single/combined mechanisms)

In this section, an attempt is made to understand and correlate the transitions of mechanisms among the case matrix of different parameters (see Fig. 12).

Beginning with wellbore heating, it is observed that, initially, fluid flow acts as the dominant mechanism for low values of thermal stimulation. However, for higher values of thermal stimulation, a shift in mechanism is observed. The transition from fluid flow to heat transfer occurs on account of pressure reaching equilibrium within the reservoir. Further, it's observed that even though for higher values of wellbore heating, dissociation does play a part in governing the dissociation. However, heat transfer still plays a major role in governing the dissociation within the hydrate reservoir.

In the case of thermal conductivity, it is inferred that fluid flow plays a critical role in the progression of dissociation front within the reservoir in a stable non-piston-like dissociation mode. However, with increasing thermal conductivity, the heat diffusion progresses deeper within the reservoir. As a result, dissociation, unlike previous cases, occurs on account of the dissociation mechanism. This is exactly what is observed in the result for cases b3 and b4, where an extended non-piston-like dissociation front is formed.

For depressurization cases, it's observed that the dissociation front is governed by heat transfer alone as the limiting mechanism for small depressurization driving force. This is reflected in piston-like dissociation front for case c1. However, for a much larger driving force of depressurization, it is observed that fluid flow mechanism followed by dissociation emerges as the contributing mechanisms for depressurization. The transition of these mechanisms is reflected in the extended non-piston-like dissociation front.

For permeability cases, a strong pattern is observed during the course of hydrate dissociation. For high permeability case, as expected, the fluid phases are expected to move freely. However, due to a high depressurization driving force, the fluid movement within the reservoir becomes a governing mechanism due to the rapid dissociation within the reservoir in the initial stages. The explanation for such behavior is reflected in the previous section of Depressurization (cases c3 and c4). This rapid production increases the pressure leading to secondary hydrate, and consequently, fluid flow is restricted for even such high permeability. Thus we see that for case d1, dissociation along with fluid flow determines the dissociation. Moving on further toward lower permeability cases, we see that the dissociation mechanism is insignificant, whereas heat transfer plays a far more dominant role in the rest of the three cases. For intrinsic rate constant cases, it is deduced that low hydration rate constant values lead to dissociation, which is governed by dissociation and fluid flow with dissociation mechanism having a much larger magnitude than its counterpart. However, with a progressive increase in rate constant values, e2, e3, and e4, the dissociation front is confined within a much smaller range and moves in a piston-like manner and governed through heat transfer alone as the dominant mechanism.

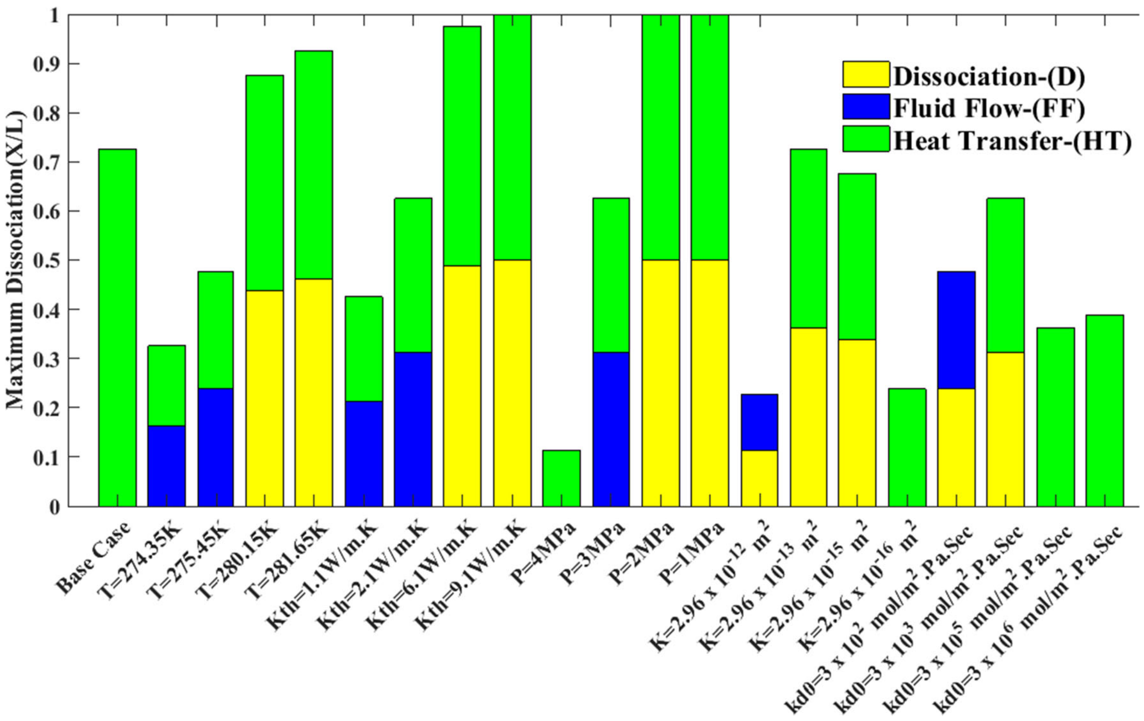

Fig. 12 Illustrating the different mechanisms associated with each of the cases

Conclusion

In the present study, through the series of simulations, the effect of different parameters, namely wellbore heating, thermal conductivity, depressurization, intrinsic permeability, and intrinsic hydration rate constant, on the hydrate dissociation using dissociation front as investigation factor is conducted. The objective is to decode the associated mechanisms such as heat transfer, dissociation, and fluid flow for each of these cases. The different cases are mathematically fitted to obtain a characteristic exponent. Next, an attempt is made to correlate the findings of associated mechanisms with their respective characteristic exponents. For this purpose, the exponents are categorized between the range of 0 to 0.5, 0.5 to 1, and few intermediary ranges to explain the mechanism transition. The detailed description is summarized in the following points below.

1) The overall energy conversion from hydrates and cumulative production is sensitive to depressurization, thermal conductivity, permeability, and wellbore heating.
2) A piston-like dissociation front is found to be associated with a single mechanism such as heat transfer. Such behavior is observed in c1, d4, e3, e4, and base cases, respectively. The range of characteristic exponent for a single heat transfer–dominated case is found to be in the vicinity of 0.6, i.e., in the range of 0.5 to 1.
3) For combination mechanisms such as heat transfer and fluid flow, in cases like a1, a2, b1, and c2, a stable non-piston-like dissociation front is formed. The characteristic exponent for such cases is found to range between 0.6 and 0.75.
4) For heat transfer and dissociation combination mechanisms, where the relative magnitude of heat transfer is higher, i.e., in cases a3, a4, b3, and b4, the characteristic exponent is found to be in close proximity to 0.5. Moreover, in such cases, the dissociation front assumes an Extended-Non-piston shape.
5) For cases like c3 and c4, where again heat transfer and dissociation mechanism combination plays the governing role, a more dominant dissociation mechanism (magnitude compared to heat transfer) pushes the characteristic exponent value to 1 (linear fitting).
6) Similar observations in terms of characteristic exponent are observed for cases d1 and e1 where dissociation mechanism magnitude is relatively larger than fluid flow, thereby pushing the characteristic exponent to 1 (linear fitting). Also, the dissociation front assumes an extended non-piston shape.

Nomenclature b, Slippage factor; c_R, Specific heat capacity of rock, [J/(kg·K)]; E_a, Activation energy, (J/mol); F_A, Area adjustment factor; f_{eq}, Equilibrium fugacity of gas phase; f_g, Fugacity of gas phase; g, Gravitational acceleration, (m/s^2); G, Gas phase denotation; H, Height of hydrate reservoir, (m); H_{dep}, Specific enthalpy of departure of gas, (J/kg); H_m, Specific enthalpy of methane in water, (J/kg); H_{isol}, Specific enthalpy corresponding to inhibitor dissolution in water, (J/kg); H_{msol}, Specific enthalpy corresponding to methane dissolution in water, (J/kg); h_{mG}, Specific enthalpy of methane in gas, (J/kg); h_w, Specific enthalpy of water in water, (J/kg); K_{Aq}, Thermal conductivity of water, [W/(m·K)]; K_G, Thermal conductivity of gas, [W/(m·K)]; K_H, Thermal conductivity of hydrate, [W/(m·K)]; K_I, Thermal conductivity of ice, [W/(m·K)]; K_R, Thermal conductivity of rock, [W/(m·K)]; K_{id}, Absorption distribution coefficient, (m^3/kg); k_{d0}, Intrinsic reaction rate of hydrate, [mol/(m^2·Pa·s)]; k, Intrinsic permeability, (m^2); k_{rAq}, Relative permeability of water; k_{rg}, Relative permeability of gas; L, Hydrate reservoir length, (m); M_m, Molecular weight of CH_4, (g/mol); M_w, Molecular weight of H_20, (g/mol); N, Hydration number (6); P_{Aq}, Pressure exerted by water phase, (Pa); P_{eq}, Equilibrium pressure of hydrate, (Pa); P_G, Pressure exerted by gas phase, (Pa); q_d, Heat injection rate, (W); q_I, Water injection rate of water, (m^3/s); R, Gas constant; S_{Aq}, Saturation of water (fraction); S_G, Saturation of gas (fraction); S_H, Saturation of hydrate (fraction); S_I, Saturation of ice (fraction); T, Temperature of reservoir, (°C); t, Time, (seconds); U_{dep}, Specific internal energy of departing gas mixture, (J/kg); u_{mG}, Specific internal energy of CH4 in gas phase, (J/kg); u_{wG}, Specific internal energy of H2O in gas phase, (J/kg); u_H, Specific internal energy of gas hydrate, (J/kg); u_I, Specific internal energy of ice, (J/kg); u_m, Specific internal energy of CH4 in water phase, (J/kg)

Acknowledgements This work is supported by the Gas Hydrate Research & Technology Centre (*GHRTC*) through the Oil and Natural Gas (ONGC), Panvel, and Ministry of Human Resource Development (MHRD), India.

Declarations

Conflict of interest The author(s) declare that they have no competing interests.

References

Ahmadi G, Ji C, Smith DH (2007a) Production of natural gas from methane hydrate by a constant downhole pressure well. Energy Convers Manag 48:2053–2068. https://doi.org/10.1016/j.enconman.2007.01.015

Ahmadi G, Ji C, Smith DH (2007b) Natural gas production from hydrate dissociation: an axisymmetric model. J Pet Sci Eng 58:245–258. https://doi.org/10.1016/j.petrol.2007.01.001

Azizi MA, Brouwer J, Dunn-Rankin D (2016) Analytical investigation of high temperature 1 kW solid oxide fuel cell system feasibility in methane hydrate recovery and deep ocean power generation. Appl Energy 179:909–928. https://doi.org/10.1016/j.apenergy.2016.06.119

Bai Y, Li Q (2010) Simulation of gas production from hydrate reservoir by the combination of warm water flooding and depressurization. Sci China Technol Sci 53:2469–2476. https://doi.org/10.1007/s11431-010-4036-y

Castaldi MJ, Zhou Y, Yegulalp TM (2006) Down-hole combustion method for gas production from methane hydrate. J Pet Sci Eng 56:44–55. https://doi.org/10.1016/j.petrol.2006.03.031

Du Q-J, Chen Y-M, Li S et al (2007) Mathematical model for natural gas hydrate production by heat injection. Shiyou Kantan Yu Kaifa/Petroleum Explor Dev 34

Du Y, He S, Huang C, Feng Z (2008) Experimental studies of natural gas hydrate formation and dissociation in porous media with 2D experimental system. J Chem Ind Eng

Hamaguchi R, Nishimura Y, Inoue G, Matsukuma Y, Minemoto M (2007) Gas hydrate decomposition rate in flowing water. J Energy Resour Technol Trans ASME 129:102–106. https://doi.org/10.1115/1.2718579

Hong H, Pooladi-Darvish M (2018) A numerical study on gas production from formations containing gas hydrates. Can Int Pet Conf 2003, CIPC 2003. https://doi.org/10.2118/2003-060

Hong H, Pooladi-Darvish M, Bishnoi PR (2003) Analytical modelling of gas production from hydrates in porous media. J Can Pet Technol 42:45–56. https://doi.org/10.2118/03-11-05

Jamaluddin AKM, Kalogerakis N, Bishnoi PR (1989) Modelling of decomposition of a synthetic core of methane gas hydrate by coupling intrinsic kinetics with heat transfer rates. Can J Chem Eng 67:948–954. https://doi.org/10.1002/cjce.5450670613

Ji C, Ahmadi G, Smith DH (2001) Natural gas production from hydrate decomposition by depressurization. Chem Eng Sci 56:5801–5814. https://doi.org/10.1111/nup.12190

Kim HC, Bishnoi PR, Heidemann RA, Rizvi SSH (1987) Kinetics of methane hydrate decomposition. Chem Eng Sci 42:1645–1653

Konno Y, Oyama H, Nagao J, Masuda Y, Kurihara M (2010) Numerical analysis of the dissociation experiment of naturally occurring gas hydrate in sediment cores obtained at the eastern Nankai Trough, Japan. Energy Fuel 24:6353–6358. https://doi.org/10.1021/ef1008727

Li B, Sen LX, Li G et al (2014) Depressurization induced gas production from hydrate deposits with low gas saturation in a pilot-scale hydrate simulator. Appl Energy 129:274–286. https://doi.org/10.1016/j.apenergy.2014.05.018

Li S, Li S, Pang W (2020) Description of gas hydrate using digital core technology. J Energy Resour Technol Trans ASME 142. https://doi.org/10.1115/1.4045533

Li XS, Wang Y, Duan LP et al (2012) Experimental investigation into methane hydrate production during three-dimensional thermal huff and puff. Appl Energy 94:48–57. https://doi.org/10.1016/j.apenergy.2012.01.024

Moridis GJ (2003) Numerical studies of gas production from methane hydrates. In: SPE Journal. pp 359–370

Rice W (2003) Proposed system for hydrogen production from methane hydrate with sequestering of carbon dioxide hydrate. J Energy Resour Technol Trans ASME 125:253–257. https://doi.org/10.1115/1.1615795

Selim MS, Sloan ED (1990) Hydrate dissociation in sediment. Soc Pet Eng AIME, SPE 5:27–30. https://doi.org/10.2118/16859-pa

Selim MS, Sloan ED (1985) Modeling of the dissociation of an in-situ hydrate. In: Society of Petroleum Engineers - SPE California Regional Meeting, CRM 1985. pp 75–80

Selim MS, Sloan ED (1989) Heat and mass transfer during the dissociation of hydrates in porous media. AICHE J 35:1049–1052. https://doi.org/10.1002/aic.690350620

Shi B, Liu Y, Ding L, Lv X, Gong J (2018) New simulator for gas-hydrate slurry stratified flow based on the hydrate kinetic growth model. J Energy Resour Technol Trans ASME 141, 141. https://doi.org/10.1115/1.4040932

Takano O, Nishimura M, Fujii T, Saeki T (2009) Sequence stratigraphic distribution analysis of methane-hydrate-bearing submarine-fan turbidite sandstones in the eastern Nankai Trough area: relationship between turbidite facies distributions and BSR occurrence. Chigaku Zasshi (J Geogr) 118:776–792. https://doi.org/10.5026/jgeography.118.776

Tsypkin G (1991) Effect of liquid phase mobility on gas hydrate dissociation in reservoirs. Fluid Dyn 26:564–572. https://doi.org/10.20595/jjbf.19.0_3

Tsypkin GG (1993) Mathematical model of the dissociation of gas hydrates coexisting with ice in natural reservoirs. Fluid Dyn 28:223–229. https://doi.org/10.1007/BF01051211

Uddin M, Coombe D, Law D, Gunter B (2008a) Numerical studies of gas hydrate formation and decomposition in a geological reservoir. J Energy Resour Technol Trans ASME 130:0325011–03250114. https://doi.org/10.1115/1.2956978

Uddin M, Coombe D, Wright F (2008b) Modeling of CO2-hydrate formation in geological reservoirs by injection of CO_2 gas. J Energy Resour Technol Trans ASME 130:0325021–03250211. https://doi.org/10.1115/1.2956979

Ullerich JW, Selim MS, Sloan ED (1987) Theory and measurement of hydrate dissociation. AICHE J 33:747–752. https://doi.org/10.1002/aic.690330507

Yousif MH, Abass HH, Selim MS, Sloan ED (1991) Experimental and theoretical investigation of methane-gas-hydrate dissociation in porous media. SPE Reserv Eng (Society Pet Eng) 6:69–76. https://doi.org/10.2118/18320-PA

Yousif MH, Li PM, Selim MS, Sloan ED (1990) Depressurization of natural gas hydrates in berea sandstone cores. J Incl Phenom Mol Recognit Chem 8:71–88. https://doi.org/10.1007/BF01131289

Zhang X, Liu Y, Li Q et al (2010) The dissociation scope of gas hydrate in deposit around heat conductor. Mech Eng 32:39–41